

# A Tale of Seemingly “Identical” Silicon Quantum Dot Families: Structural Insight into Silicon Quantum Dot Photoluminescence

Alyxandra N. Thiessen, Lijuan Zhang, Anton O. Oliynyk, Haoyang Yu, Kevin M. O’Connor, Alkiviathes Meldrum, and Jonathan G. C. Veinot\*



Cite This: *Chem. Mater.* 2020, 32, 6838–6846



Read Online

ACCESS |



Metrics & More

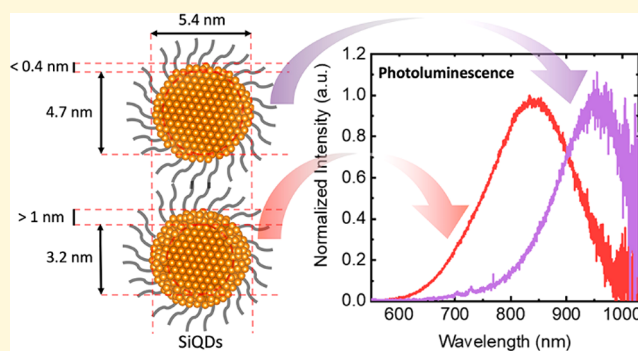


Article Recommendations



Supporting Information

**ABSTRACT:** “Two quantum dots, both alike in composition, but differing in structure, where we lay our scene, From broader classes, to bring deeper understanding, to the crystalline core that drives the quantum dot’s sheen.” In this contribution we examine two families of silicon quantum dots (SiQDs) that bring to mind the Capulets and the Montagues in Shakespeare’s *Romeo and Juliet* because of their stark similarities and differences. SiQDs are highly luminescent, heavy-metal-free, and based upon earth-abundant elements. As such, they have attracted attention for far-reaching applications ranging from biological imaging to luminescent solar concentrators to light-emitting diodes that rely on their size-dependent optical response. Unfortunately, correlating SiQDs “size” to their photoluminescence (PL) maximum is often challenging. Herein, we provide essential structural insight into the correlation between the dimensions and PL maximum of SiQDs through a direct comparison of samples that exhibit statistically identical physical dimensions ( $d_{\text{TEM}}$ ) and chemical compositions but different crystallite size ( $d_{\text{XRD}}$ ) and PL maxima. We then expand the scope of this investigation and systematically compare groupings of SiQDs: one in which the  $d_{\text{XRD}}$  and  $d_{\text{TEM}}$  agree and one where  $d_{\text{XRD}} < d_{\text{TEM}}$ . This latter comparison clearly shows that  $d_{\text{XRD}}$  better predicts SiQD optical response when using the well-established effective mass approximation.



Semiconductor nanoparticles (quantum dots, QDs) are fascinating structures that exhibit size- and shape-dependent optoelectronic properties. Prototypical CdSe@ZnS QDs have been widely studied and are generally well-understood, and many reports of prototype applications have appeared; in fact, InP-based QDs are revolutionizing consumer electronics as active systems in QLED-TV displays.<sup>1,2</sup> Unfortunately, legislation limits the use of heavy metals in consumer products and curtails widespread implementation of many QDs,<sup>3</sup> furthermore, alternative QD materials such as InP contain costly non-earth-abundant elements and exhibit “clear evidence of carcinogenic activity” in animal models.<sup>4</sup> In this context, QDs comprised of abundant, nontoxic elements must be prepared, manipulated, understood, and deployed.<sup>5</sup>

Silicon-based QDs (SiQDs) are attractive for many applications because they are heavy-metal-free, comprised of earth-abundant elements, and are biologically compatible. In this context, a variety of methods have been developed to prepare and functionalize these promising materials,<sup>6–11</sup> and prototype applications, including light-emitting diodes,<sup>12</sup> luminescent solar concentrators (LSCs),<sup>13,14</sup> biological imaging agents,<sup>15,16</sup> sensors,<sup>17,18</sup> and lithium ion battery anodes,<sup>19,20</sup> have appeared. Many of these uses rely on the unique tailorable optical properties of SiQDs; for example, LSCs take advantage of the large Stokes shift (i.e., the energy difference

between excitation and photoluminescence maxima) that arises in part because of the indirect nature of the Si band gap.<sup>13,14</sup> Despite impressive advances, including spectral tuning throughout the full visible region and photoluminescence (PL) quantum yields rivaling that of compound semiconductor QDs, challenges remain;<sup>21–25</sup> paramount among these is the limited predictability of the PL maximum size dependence that appears throughout the literature.<sup>26</sup>

The origin of SiQD PL is clearly complex,<sup>27–32</sup> for convenience, SiQDs can be categorized into two broad groupings based upon PL properties and associated excited-state lifetimes.<sup>28</sup> The first involves SiQDs exhibiting PL characterized by short-lived excited states (i.e.,  $\tau$  = nanoseconds); in these cases the PL maximum that often appears in the blue spectral region (i.e., 390–500 nm) is dependent on excitation wavelength and largely independent of particle size. Such behavior has previously been attributed to surface-state-

Received: February 14, 2020

Revised: June 26, 2020

Published: June 29, 2020



mediated relaxation processes involving heteroatom-containing species (e.g., N, Cl, O, etc.).<sup>21,28,29,33–35</sup> Other SiQDs show PL throughout the yellow/orange to near-IR regions with long-lived excited states (i.e.,  $\tau$  = microseconds) consistent with the indirect band gap of silicon; the proposal that this luminescence arises from band-gap-based processes is further supported as the PL maximum generally trends with particle size and is broadly consistent with carrier quantum confinement.<sup>25,29,33,36</sup>

A comprehensive review of SiQDs exhibiting microsecond lifetimes has appeared, and a detailed discussion is beyond the scope of the present contribution.<sup>33</sup> However, for context it is useful to consider that while the PL response of these QDs has been attributed to carrier confinement, the PL maximum of seemingly identical particles can vary greatly and its energy frequently does not correlate well with effective mass approximation (EMA) predictions (Figure 1).<sup>26,37–39</sup> Numer-

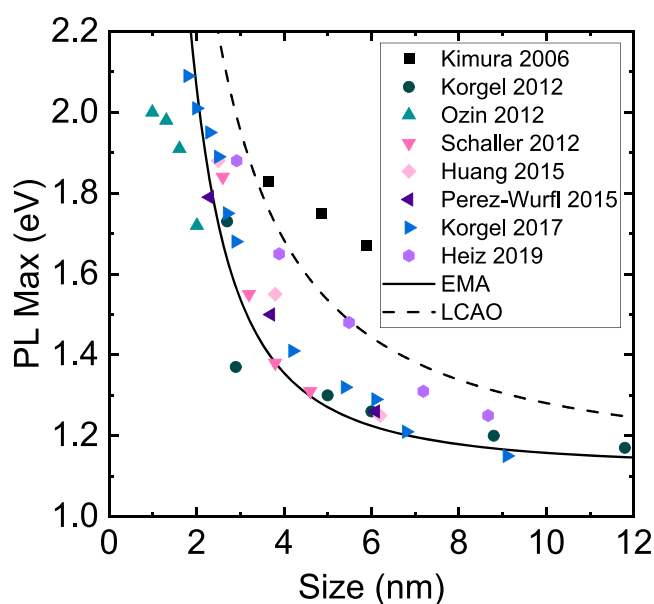


**Figure 1.** A summary of representative literature data showing the relationship between SiQD peak PL emission and particle dimension.<sup>37,39,40,47–51</sup> Predicted relationships obtained using the effective mass approximation (EMA)<sup>52</sup> [solid line;  $E_g(r) = 1.12 + 3.77/r^2$ ] and linear combination of atomic orbitals (LCAO)<sup>26,42</sup> [dashed line;  $E_g(r) = 1.12 + 3.77/r^{1.39}$ ] are shown for comparison.

ous explanations for these deviations have appeared, such as broad particle size distributions,<sup>40</sup> among others.<sup>38,41</sup> As such, alternative strategies [e.g., empirical pseudopotential approximation (linear combination of atomic orbitals, LCAO),<sup>42,43</sup> empirical tight binding band theory,<sup>44,45</sup> and ab initio local density approximation]<sup>46</sup> for correlating the PL maximum to SiQD dimensions have been proposed.<sup>26,38,39,42</sup>

It is well-established that many challenges (as well as intriguing properties) associated with preparing and exploiting SiQDs arise from the extended covalent bonding manifested within the Si diamond-like crystal structure. While amorphous surface layers have been implicated in ultrafast SiQD photoluminescence,<sup>53–56</sup> the uniformity of the SiQD internal structure has largely been overlooked.<sup>57</sup> We previously demonstrated that the Si core of large ( $d_{\text{TEM}} \sim 9\text{--}64$  nm) SiQDs exhibits a radially graded structure consisting of a highly disordered surface that transitions to a crystalline core; in

contrast, the structure of small SiQDs ( $d_{\text{TEM}} \sim 3$  nm) is dominated by disorder and they only possess very small crystallite regions (i.e.,  $d_{\text{XRD}} \sim 1.2$  nm).<sup>57</sup> Knowing that the electronic structure of bulk silicon strongly depends on crystallinity (e.g., amorphous Si  $E_{g,\text{optical}} = 1.6\text{--}1.7$  eV; bulk crystalline Si  $E_g = 1.1$  eV),<sup>58</sup> we endeavored to explore the impact of internal structure on SiQD optical response. Herein, we describe an evaluation of the size dependence of the SiQD PL maximum and excited-state lifetime while systematically varying particle and crystallite sizes, as determined by transmission electron microscopy (TEM) and X-ray powder diffraction (XRD), respectively.

## RESULTS AND DISCUSSION

To probe the impact of an internally graded crystal structure on SiQD optical properties it was necessary to predictably prepare QDs with the same particle sizes (determined using TEM;  $d_{\text{TEM}}$ ) and different crystallite sizes (determined using XRD,  $d_{\text{XRD}}$ ) while maintaining all other contributing factors (e.g., surface chemistry/oxidation) the same. Drawing on our intimate knowledge of the hydrogen silsesquioxane (HSQ)-based procedure and the structure of the resulting SiQDs,<sup>57,59–61</sup> we prepared two different composites consisting of nanocrystalline silicon domains encased within an SiO<sub>2</sub>-like matrix via HSQ reductive thermal processing at 1200 and 1300 °C. Evaluation of the Si domain sizes using TEM was precluded by the oxide matrix; however, consistent with expectation,<sup>37,60</sup> XRD revealed reflections attributable to nanocrystalline Si domains, and as expected, it revealed larger domains for products processed at higher  $T$  (i.e.,  $d_{1200} \sim 3.7$  nm,  $d_{1300} \sim 6.1$  nm).

Freestanding SiQDs were liberated from an HSQ-derived SiO<sub>2</sub>-like matrix upon etching with alcoholic aqueous hydrofluoric acid. Drawing on the reasonable expectation that amorphous/disordered silicon is more susceptible to this etching process, the definition of the etching time allowed isolation of SiQDs from the composites that possess statistically identical  $d_{\text{TEM}}$  but different  $d_{\text{XRD}}$  dimensions (i.e., different thicknesses of disordered Si shells). As a result of experimental variations of the SiQD/SiO<sub>2</sub> composite, it is important to qualitatively monitor the appearance/color of the etching mixture. Doing so provides a qualitative indication of the SiQD size (i.e.,  $d \sim 2.5$  nm, yellow;  $d \sim 3$  nm, yellow/orange;  $d \sim 5$  nm, orange; not freestanding, brown/black); however, the exact etching time depends on the specific composite and all SiQDs must be characterized following surface functionalization using quantitative methods (*vide infra*) to confirm their dimensions.

Following isolation, the SiQDs were surface-functionalized using size-independent radical-induced hydrosilylation to render them solution-processable and minimize reactions (e.g., oxidation) that are known to deleteriously impact optical response.<sup>11</sup> Fourier-transform infrared spectra of the resulting materials are consistent with successful functionalization and show the features expected for surface-bonded dodecyl moieties [Figure S1, Supporting Information (SI)].<sup>11</sup> For the following discussion, SiQDs resulting from composites prepared at 1200 and 1300 °C will be referred to as 1200-SiQD and 1300-SiQD, respectively.

Prior to evaluating the size and optical properties of the SiQDs, it is essential to confirm that the degree and speciation of surface oxidation is consistent across the samples, because these factors can also impact SiQD PL response.<sup>29,62</sup> To do so,

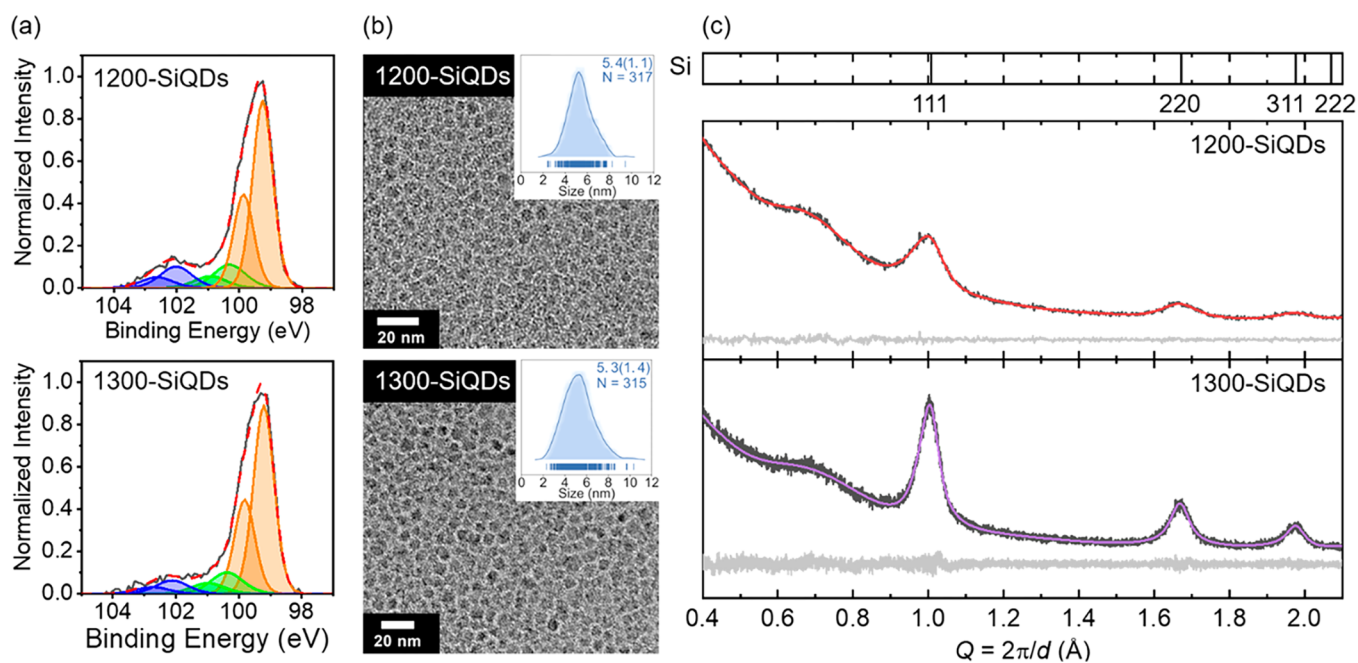


**Figure 2.** (a) Si 2p XP spectrum with deconvolution/fitting of the data for 1200-SiQDs and 1300-SiQDs. Fitting peaks are shown as Si  $2p_{1/2}$  and  $2p_{3/2}$  components corresponding to Si(0) (i.e., orange), Si(I) (i.e., green), and Si(II) (i.e., blue). The black trace is the experimental spectrum and the red dashed line represents the overall fitting envelope. (b) TEM image of 1200-SiQDs and 1300-SiQDs. Inset: average shifted histogram with the average size and the distribution width. (c) XRD data for 1200-SiQDs and 1300-SiQDs showing the experimental powder pattern (black) with fitting (red for 1300-SiQDs and purple for 1200-SiQDs) and residuals (light gray).

the Si 2p XP spectra of the 1200- and 1300-SiQDs (Figure 2a) were deconvoluted into component spin–orbit couples (Si  $2p_{1/2}$  and  $2p_{3/2}$ ) corresponding to Si(0) (i.e., orange), Si(I) (i.e., green), and Si(II) (i.e., blue).<sup>57</sup> Integrating the total area of the Si(I) and Si(II) components and comparing it to the integrated area of the Si(0) component provided an estimation of the ratio of oxidized surface silicon species to elemental silicon. For the present samples, the total integrated signal of the Si(I) and Si(II) components corresponds to 21% for 1300-SiQDs and 27% for 1200-SiQDs of the total Si 2p signal intensity. This, combined with the reasonable assumption that the degree of surface functionalization (i.e., surface density of Si–C bonds) is equivalent for both samples, indicates that the 1200- and 1300-SiQDs have similar amounts of oxidation. Furthermore, closer inspection of the O and Si spectral envelopes indicates that the speciation of the oxides is near identical. In this context, we expect the influence (if any) of surface oxide species on the optical properties of 1200- and 1300-SiQDs to be similar.

Turning to the evaluation of QD particle and crystallite sizes, a side-by-side comparison of sample size distributions obtained from HAADF-STEM and bright-field TEM (see Figure S2, SI) was statistically identical at the 0.05 confidence level when evaluated using a two-sided *t* test. Upon the basis of this fact, bright-field TEM analysis was chosen to evaluate the liberated dodecyl-functionalized particles. This analysis afforded  $d_{\text{TEM}}$  of  $5.3 \pm 1.4$  and  $5.4 \pm 1.1$  nm (Figure 2b) for the 1200- and 1300-SiQDs, respectively, and they are statistically similar to a 95% confidence interval. To complement the TEM analyses, crystallite sizes of the identical samples were determined using XRD. Diffraction data were fit to the NIST Si line shape standard (640f) as an “infinite” crystallite reference to account for instrumental broadening and line shape. Having accounted for instrumental broadening and Gaussian and Lorentzian peak

shape parameters, with the assumption that atomic displacement parameters and crystallographic site deficiencies do not play a role, only size and strain contributions to line broadening remain and can be qualitatively accounted for on the basis of their diffraction angle dependence.<sup>57,63</sup> In contrast to the  $d_{\text{TEM}}$  values, which were statistically identical, the  $d_{\text{XRD}}$  values (i.e., crystallite sizes) determined from diffraction data (Figure 2c) were  $3.2 \pm 1.22$  and  $4.7 \pm 0.4$  nm for 1200-SiQDs and 1300-SiQDs, respectively. A straightforward comparison of the  $d_{\text{TEM}}$  and  $d_{\text{XRD}}$  clearly shows that, despite having the same physical dimensions, 1200-SiQDs have a smaller crystallite size (and by extension thicker disordered Si shell). This is further supported by high annular angle dark field scanning transmission electron microscopy (HAADF-STEM) that shows thicker disordered layers on 1200-SiQDs (1.7 nm for 1200-SiQDs vs 1.0 nm for 1300-SiQDs; Figures S3 and S4, SI). Our data analyses reasonably assume that the bright area in the HAADF-STEM images is representative of the overall SiQD size without the organic ligand (which has a lower Z-contrast compared to the silicon) and that the lattice fringes are representative of the dimensions of the crystalline core. With these caveats, the difference in the dimensions of these particles indicates a thicker disordered layer on the 1200-SiQDs.

Having shown that 1200-SiQDs and 1300-SiQDs exhibit near-identical physical size (i.e.,  $d_{\text{TEM}}$ ) as well as composition (i.e., degree of oxidation, oxidation speciation, surface functionalization) and differ only in the size of the crystalline core (i.e.,  $d_{\text{XRD}}$ ), we endeavored to evaluate the impact of the disordered Si shell on the optical properties of 1200-SiQDs. The PL spectra of SiQD toluene solutions (Figure 3a) were evaluated using the 351 and 364 nm lines of an Ar ion laser and show maxima of 837 and 955 nm for 1200-SiQDs and 1300-SiQDs, respectively. The marked red-shift in PL

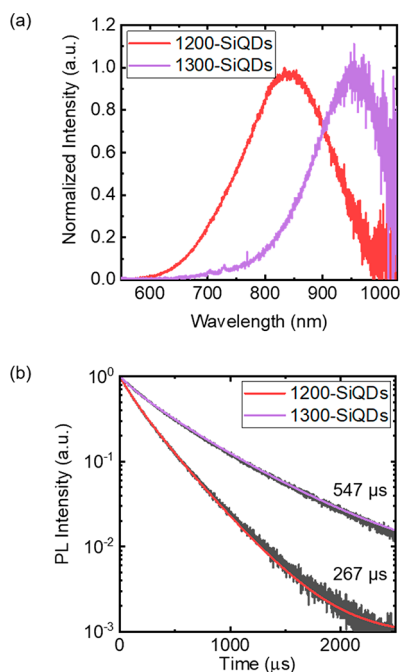


**Figure 3.** Comparing (a) the photoluminescence emission of 1300-SiQDs (purple) and 1200-SiQDs (red), as well as (b) the luminescence lifetimes of 1300-SiQDs (purple fit) and 1200-SiQDs (red fit). Photoluminescence emission data were collected on an Ocean Optics 2000+ spectrometer. Luminescence lifetimes were fit to a stretched exponential function and the mean time constants were then calculated as described below.<sup>64</sup> The fitting parameters are reported in Table S2 (SI).

maximum with increased  $d_{\text{XRD}}$  suggests that the dimensions of the nanocrystalline domain dominate SiQD PL and band gap; there is no demonstrable indication of a contribution from the disordered surface silicon species to these properties. This observation is consistent with the amorphous silicon shell having a wider band gap than the crystalline core, providing a core@shell structure similar to that of more commonly studied CdSe@ZnS systems (i.e., type I QDs).<sup>65</sup> Contrary to the CdSe@ZnS QD case, in which the ZnS shell grows epitaxially on the CdSe core to reduce interfacial dark defects and increase the PL QY, the graded interface between the crystalline and amorphous components of the present SiQDs can reasonably be expected to be ill-defined.<sup>57,66,67</sup> As such, there is no obvious trend in the present PL QY data for the core@shell systems (Figure S7, SI).

Time-resolved photoluminescence (TRPL) traces were fit with a stretched exponential model given by

$$I_t = A \exp[-(t/\tau)^\beta] + dc \quad (1)$$

From the  $\beta$  and  $\tau$  fitting parameters, the mean time constant (referred to henceforth as the mean lifetime) was obtained according to

$$\bar{\tau} = \tau \frac{\Gamma(2/\beta)}{\Gamma(1/\beta)} \quad (2)$$

This model has been widely applied to SiQDs and tends to fit the TRPL data quite well for the purposes of extracting a mean lifetime.<sup>64</sup> The 1300-SiQDs exhibit a longer mean lifetimes (i.e., 547  $\mu\text{s}$  for 1300-SiQDs vs 267  $\mu\text{s}$  for 1200-SiQDs), consistent with experimental reports<sup>48</sup> and models<sup>72</sup> showing longer lifetimes for larger SiQDs. Upon examining the mean

lifetimes of all of the SiQDs here studied as a function of PL energy, an obvious trend was observed where  $\frac{1}{\bar{\tau}} = A' e^{E/E_0}$  (Figure 4;  $A' = 62.5 \text{ s}^{-1}$  and  $E_0 = 0.34 \text{ eV}$ ). This trend is consistent across literature,<sup>69,70</sup> is independent of synthetic method and has been implicated with the indirect band gap of silicon.<sup>68</sup>

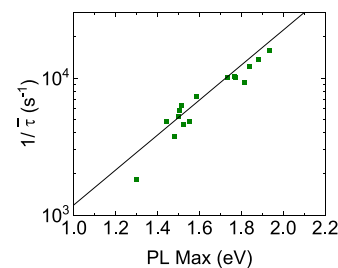


**Figure 4.** A plot of the maximum photoluminescence energy against the lifetimes for all SiQDs in this study. A clear trend is observed that can be fit to the equation  $\frac{1}{\bar{\tau}} = A' e^{E/E_0}$ ,<sup>68–70</sup> where  $A' = 62.5 \text{ s}^{-1}$  and  $E_0 = 0.34 \text{ eV}$  (the black line).

To further explore the broader scope of the relationship between SiQD optical properties and  $d_{\text{XRD}}$ , SiQD/SiO<sub>2</sub> composites were prepared via reductive thermal processing of HSQ at 1100, 1200, and 1300 °C, in order to have a wider range of Si crystallite sizes.<sup>37,60</sup> SiQDs were liberated upon alcoholic HF etching for predetermined times (see Table S1, SI) and surface-functionalized with Si–C tethered 1-dodecyl surface groups via AIBN radical-initiated hydrosilylation. Subsequently, the  $d_{\text{TEM}}$ ,  $d_{\text{XRD}}$ , and PL properties were evaluated and compared. This method yielded SiQDs with varying disordered layer thicknesses, where in all cases the  $d_{\text{TEM}}$  is larger than  $d_{\text{XRD}}$  (Figure S8, SI).

To better illustrate/understand the relationship between SiQD dimensions and optical properties, we categorized the present data into two groups: (1) samples in which the  $d_{\text{TEM}}$  is substantially larger than  $d_{\text{XRD}}$  (i.e.,  $d_{\text{TEM}} - d_{\text{XRD}} > 2 \text{ nm}$ ). (These particles possess comparatively thick amorphous/disordered Si layers on their surfaces.) and (2) samples for which  $d_{\text{TEM}}$  and  $d_{\text{XRD}}$  are similar (i.e.,  $d_{\text{TEM}} - d_{\text{XRD}} < 0.8 \text{ nm}$ ) (These particles possess a thin amorphous/disordered Si layer on their surfaces.). Data were subsequently plotted and compared with the predictions of the effective mass approximation (EMA; Figure 5c,d).

Consistent with our previous observations (see above), there is a clear correlation between  $d_{\text{XRD}}$  and EMA predictions for the photoluminescence of SiQDs in group 1 (i.e.,  $d_{\text{TEM}} - d_{\text{XRD}} > 2 \text{ nm}$ ; Figure 5c)—this is not the case for  $d_{\text{TEM}}$ . We also note that the EMA consistently overestimates particle size when comparing to  $d_{\text{XRD}}$ . In contrast, for group 2, SiQDs that bear a thin amorphous Si layer, the PL emission energy is closely related to  $d_{\text{XRD}}$  and  $d_{\text{TEM}}$  (Figure 5d); furthermore, the EMA appears to agree better with the data. We also note similar relationships when evaluating time-resolved photoluminescence data in the context of  $d_{\text{TEM}}$  and  $d_{\text{XRD}}$ . To investigate the effect of the size distribution on the mean luminescence energies, we tested a model similar to that reported in ref 39. For particles with the same annealing temperature, and thus presumably similar defect distributions and shell thickness, we find that a somewhat better match to the XRD data can be obtained if the size distribution is factored into the analysis

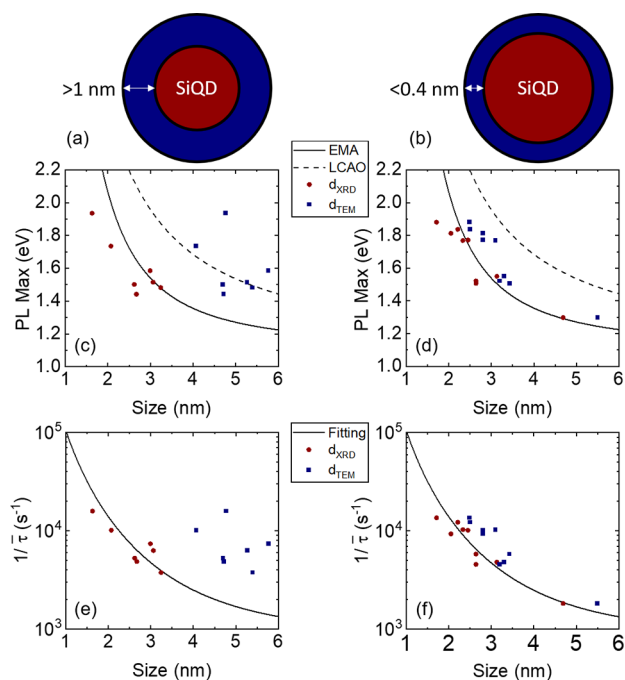


**Figure 5.** A schematic representation of Si QDs showing the thick (a) and thin (b) amorphous layers surrounding the crystalline core. A comparison of the relationship between PL energy (c and d) and lifetimes (e and f) with  $d_{\text{TEM}}$  (blue squares) and  $d_{\text{XRD}}$  (red circles) for SiQDs with a thick amorphous layer (>1 nm; a, c, e) and a thin amorphous layer (<0.4 nm; b, d, f). The solid and dashed black lines in parts c and d represent the EMA and LCAO as in Figure 1. The solid black line in parts e and f is a fitting from all of the  $d_{\text{XRD}}$  vs lifetime data according to eq 3.

(Figure S15, SI). It is important to note that the impact of the size distribution is not as obvious for the materials presented here when compared to those reported in ref 39 because the SiQDs reported previously were isolated through size-selected precipitation (i.e., they have narrow size distributions) and they likely have no disordered shell due to the extended etching process employed.

Theory predicts that the radiative lifetime of a silicon nanocrystal scales approximately as the inverse cube of the radius.<sup>71,72</sup> Thus, the mean lifetime data were fit to an inverse cubic function of the XRD radius by

$$\frac{1}{\tau} = A'' \left( \frac{1}{d_{\text{XRD}}} \right)^3 + C \quad (3)$$

where  $A'' = 0.105 \text{ nm}^3 \text{ s}^{-1}$  and  $C = 8.55 \times 10^{-4} \text{ s}^{-1}$ , which appeared to yield a good fit to the experimental data (Figure 5e,f). Of course, there is also a strong nonradiative contribution that cannot be measured directly; however, under certain specific conditions (i.e., for a single defect) the dominant nonradiative decay rate also scales inversely with the crystallite volume.<sup>73</sup> Obviously, the actual nonradiative rate depends on the abundance and types of defects present in the samples, which may differ and likely explains some of the differences between the data and the model shown in Figure 5e,f.

The direct relationship between theoretical PL energy and lifetimes and the crystallite diameter of these SiQDs, especially when they have a thin amorphous layer (group 2), suggests that the crystalline core controls the optical response.

However, the relationships among SiQD luminescence, graded structure, and size presented for group 1 are similar to those previously noted for CdSe@CdSe<sub>x</sub>S<sub>1-x</sub>@CdS QDs, in which the confinement of carriers (i.e., electrons and holes) depends upon a radially varied structure.<sup>74</sup> A detailed study of the interplay of these factors in the SiQD optical behavior is obviously complicated by the poorly defined nature of the transitional region between the crystalline core and amorphous shell; however, one can expect that the confinement should be stronger when the shell is thinner, as implied by the results in Figure 4. This clearly highlights the importance (and promise) of establishing methods for controlling the uniformity of the internal SiQD structure, as well as preparing well-defined core@shell SiQD systems.

## CONCLUSION

In conclusion, the photoluminescence of functionalized SiQDs has been evaluated in the context of internal crystallinity by examining crystallite and particle dimensions using X-ray diffraction and transmission electron microscopy. For SiQDs prepared via the widely employed “HSQ method”, the  $d_{\text{XRD}}$  provides a better representation of the optically active QD dimensions, regardless of the presence of an amorphous overlayer. In cases in which a thick Si amorphous layer is present, no obvious correlation between  $d_{\text{TEM}}$  and the photoluminescence is noted. However, EMA estimates derived from  $d_{\text{TEM}}$  and  $d_{\text{XRD}}$  dimensions agree reasonably well with the data when thin amorphous Si layers are present. This fundamental understanding of SiQD structure and its influence on their luminescence properties illuminates a foundation on which future efforts to better control SiQD optical response can be constructed.

## EXPERIMENTAL SECTION

**Materials. Reagents.** Hydrofluoric acid (electronic grade, 48–50%) was purchased from Fischer Scientific. Sulfuric acid (reagent grade, 95–98%) was purchased from Caledon Laboratory Chemicals. Fuming sulfuric acid (reagent grade, 20% free SO<sub>3</sub> bases) and trichlorosilane (99%) were purchased from Sigma (now MilliporeSigma). All reagents were used as received unless otherwise specified. All solvents were reagent grade and used as received. Toluene was collected from a Pure-Solv purification system immediately prior to use. Benzene was purchased from EMD Millipore (now Millipore Sigma).

**Preparation of Hydrogen Silsesquioxane (HSQ).** HSQ was synthesized via known literature procedures in which sulfuric acid is used to selectively oxidize trichlorosilane. Dry toluene (45.0 mL) was added to a mixture of concentrated (15.0 mL) and fuming (7.2 mL) sulfuric acid under inert atmosphere. Once the addition was complete, 110 mL of dry toluene was added to 16 mL of trichlorosilane and added dropwise over a few hours to the sulfuric acid solution. The product dissolved in the organic layer was washed with sulfuric acid solution. After drying the organic layer, most of the toluene was removed via rotary evaporation and the rest was removed *in vacuo*. The resulting white solid was stored under vacuum until use.

**Preparation of the SiQDs/SiO<sub>2</sub> Composite.** Thermal decomposition of the HSQ, as previously reported, was used to produce the SiQDs used in this study. Six grams of HSQ was annealed in a tube furnace under a 5% H<sub>2</sub>/Ar atmosphere at 1100, 1200, and 1300 °C to get various sizes of nanocrystals (the sizes associated with each temperature can be seen in Table S1, SI). The composite was ground using an agate mortar and pestle and then shaken for 6 h to prepare a fine powder.

**Preparation of Alkyl-Passivated SiQDs.** The composite was then etched using a 1:1:1 solution of ethanol:DI water:HF to remove the SiO<sub>2</sub> matrix from the particles using 0.5 g of composite per etch and

15 mL total of etching solution. The composite was etched as described in the Supporting Information (Table S1), and the resulting particles were extracted in toluene. The hydride-terminates SiQDs (H-SiQDs) were centrifuged twice in toluene and redispersed in 10 mL of dry toluene with 6 mL of dodecene and 300 mg of AIBN. The reaction mixture was degassed using three freeze–pump–thaw cycles and placed in an oil bath at 70 °C overnight (~17 h).

The resulting SiQDs were purified via centrifugation using 10 mL of toluene and 20 mL of methanol three times to remove any unreacted dodecene and AIBN. The purified SiQDs were redispersed in toluene for subsequent characterization.

**Characterization.** *Fourier-Transform Infrared Spectroscopy.* Fourier-transform infrared spectroscopy (FTIR) was performed on a Thermo Nicolet Continuum FT-IR microscope by drop-casting SiQDs onto a silicon wafer from dry toluene solutions.

*X-ray Photoelectron Spectroscopy.* X-ray photoelectron spectroscopy (XPS) was measured using a Kratos Axis 165 Ultra X-ray photoelectron spectrometer. A monochromatic Al K $\alpha$  source operating at 210 W with an energy  $h\nu = 1486.6$  eV was used. Survey spectra were collected with an analyzer pass energy of 160 eV and a step of 0.3 eV. For high-resolution spectra, the pass energy was 20 eV and the step was 0.1 eV with a dwell time of 200 ms. XPS samples were prepared by drop-coating a dispersion of SiQDs in dry toluene onto a copper foil. Spectra were calibrated to C 1s (284.8 eV) and fit to appropriate spin–orbit pairs using CasaXPS (VAMAS) software with a Shirley-type background. To fit the Si 2p high-resolution spectrum, the doublet area ratio was fixed at 2:1 and the separation was set at 0.6.

*Electron Microscopy.* Transmission electron microscopy (TEM) and HR-TEM were performed on a JEOL JEM-ARM200CF S/TEM (Cold Field Emission Gun) electron microscope with an accelerating voltage of 200 kV using SiQDs drop-coated from a toluene solution onto a holey carbon-coated copper grid. The SiQD size was determined by averaging the size of 300 particles using ImageJ software (version 1.51j8) and plotted as an average shifted histogram as outlined previously by Buriak and co-workers.<sup>75</sup>

HAADF-STEM was performed using the same instrument and sample grids. Images were subsequently processed using a Radial Wiener Filter in the Gatan Microscopy Suite 3.0 and subjected to trend subtraction (Figure S5, SI).<sup>76</sup> The thickness of the amorphous layer was determined using ImageJ by overlaying two perpendicular lines spanning the diameter of the crystalline domain (revised Figure S5a, filtered image, SI) and the total particle diameter (revised Figure S5b) and calculating the difference. This procedure was repeated for no fewer than 20 particles for each sample.

*Powder X-ray Diffraction.* Powder X-ray diffraction was measured using a Rigaku Ultima IV multipurpose X-ray diffraction system equipped with a Cu K $\alpha$  source for most of the samples. Samples were drop-cast on a zero-background Si wafer and data were collected in a thin-film orientation. For thin-film diffraction, a parallel beam was used with a glancing angle of 0.5°. Some data were also collected at the Canadian Light Source (CLS) synchrotron, with a wavelength of 0.6892 Å, using transmission mode. These methods gave equivalent data within the errors associated with the techniques and fitting parameters. To account for instrumental effects, a diffraction pattern for the NIST Si line shape standard (640f) was acquired using the identical conditions (i.e., sample holder, size step, calibration file, etc.) employed for SiQD analyses. The standards were analyzed by fitting the width of the reflections taking into account K $\alpha_1$  and K $\alpha_2$  contributions. The fit can be found in Figure S16 (SI). Pawley fitting of powder patterns was performed using the TOPAS software package to determine the crystallite domain size using the integral breadth, fwhm, and Lorentzian broadening methods.<sup>63</sup> A sample-independent synthetic peak was required at ~22° for all measurements on the laboratory instrument, which is believed to originate from the sample holder imperfections or amorphous products/unreacted materials. Synchrotron diffraction data required other small peaks (8°, 9°, 11°, 14°, 16°, and 19°) due to imperfections in the background subtraction from the Kapton tube (sample holder).

*Photoluminescence Characterization.* Photoluminescence spectroscopy measurements were performed on a solution of silicon nanocrystals dispersed in toluene in a quartz cuvette. Silicon nanoparticles were excited using an argon ion laser with a 351 nm emission wavelength. The resulting photoluminescence was collected by an optic fiber, passed through a 500 nm long-pass filter to eliminate scattered light from the excitation source, and fed into an Ocean Optics USB2000+ spectrometer with a spectral range from 300 to 1000 nm and a sensitivity of 41 photons per count at 600 nm. The spectral response was calibrated using a reference light source from Ocean Optics. Photoluminescence lifetime measurements were acquired using an argon ion laser (351 nm, ~20 mW) modulated by an acousto-optic modulator (~50 ns response time) operated at a frequency of 200 Hz with a 50% duty cycle. The photoluminescence was fed into an optic fiber and passed through a 500 nm long-pass filter and was then incident on a Hamamatsu H7422P-50 photo-multiplier tube (PMT) interfaced with a Becker-Hickl PMS-400A gated photon counter. The photoluminescence data were collected with a total of 10 000 sweeps for good signal-to-noise ratio using 1  $\mu$ s time steps. A log-normal fitting of the data in MatLab was used to calculate the luminescence decay. The lifetimes were measured for each sample individually with peak emissions at different energies (no wavelength selection was performed).

Quantum efficiency measurements were performed using a homemade integrating sphere with a 365 nm light-emitting diode excitation source. Sample solutions were diluted to have an absorbance between 0.1 and 0.15 at 405 nm, and then they were transferred into a cuvette that was lowered into the integrating sphere on a magnetic holder, as was a distilled water blank. The photoluminescence and excitation intensities were captured through a fiber attached to the sphere and analyzed with a calibrated Ocean Optics spectrometer. The equation  $QE = (I_{PL, sample} - I_{PL, blank}) / (I_{ex, blank} - I_{ex, sample})$  was used to calculate the absolute quantum efficiency, where  $I_{PL}$  is the integrated photoluminescence intensity and  $I_{ex}$  is the excitation intensity recorded inside the sphere. The measurements were performed in quintuplicate.

## ■ ASSOCIATED CONTENT

### SI Supporting Information

The Supporting Information is available free of charge at <https://pubs.acs.org/doi/10.1021/acs.chemmater.0c00650>.

FTIR, HAADF-STEM images, disordered shell thickness histograms, and survey XPS scan for 1200-SiQDs and 1300-SiQDs; a figure showing how the disordered shell was measured on HAADF-STEM images and fitting of the NIST Si line shape standard; a comparison of the quantum efficiency and  $d_{TEM}/d_{XRD}$ ; a plot comparing  $d_{TEM}$  and  $d_{XRD}$  for all samples; Figure 5 c and d showing standard deviation ( $d_{TEM}$ ) and size error ( $d_{XRD}$ ); representative FTIR, Si 2p XPS, bright-field TEM, average shifted histograms showing size distributions, and powder XRD showing fits for samples used in Figure 5; a table of the experimental parameters; and a table of fitting parameters for the lifetime decays of 1200-SiQDs and 1300-SiQDs (PDF)

## ■ AUTHOR INFORMATION

### Corresponding Author

Jonathan G. C. Veinot – Department of Chemistry, University of Alberta, Edmonton, Alberta T6G 2G2, Canada;  
orcid.org/0000-0001-7511-510X; Email: [jveinot@ualberta.ca](mailto:jveinot@ualberta.ca)

## Authors

Alyxandra N. Thiessen – Department of Chemistry, University of Alberta, Edmonton, Alberta T6G 2G2, Canada; [orcid.org/0000-0001-9978-1422](https://orcid.org/0000-0001-9978-1422)

Lijuan Zhang – Department of Physics, University of Alberta, Edmonton, Alberta T6G 2E1, Canada

Anton O. Oliynyk – Manhattan College, Riverdale, New York 10471, United States; [orcid.org/0000-0003-0732-7340](https://orcid.org/0000-0003-0732-7340)

Haoyang Yu – Department of Chemistry, University of Alberta, Edmonton, Alberta T6G 2G2, Canada; [orcid.org/0000-0002-0748-9414](https://orcid.org/0000-0002-0748-9414)

Kevin M. O'Connor – Department of Chemistry, University of Alberta, Edmonton, Alberta T6G 2G2, Canada; [orcid.org/0000-0002-6400-6319](https://orcid.org/0000-0002-6400-6319)

Alkiviathes Meldrum – Department of Physics, University of Alberta, Edmonton, Alberta T6G 2E1, Canada; [orcid.org/0000-0001-7215-4023](https://orcid.org/0000-0001-7215-4023)

Complete contact information is available at:

<https://pubs.acs.org/10.1021/acs.chemmater.0c00650>

## Notes

The authors declare no competing financial interest.

## ACKNOWLEDGMENTS

The authors would like to thank P. Li from the University of Alberta nanoFAB for his efforts to collect the HAADF-STEM images used in this work. The Natural Science and Engineering Research Council (NSERC) of Canada Discovery Grants Program (RGPIN-2015-03896) and the University of Alberta are acknowledged for their generous research support. A.N.T. is supported by the Alberta Innovates Graduate Student Scholarship. L.Z. is supported by China Scholarship Council (2018-31010). The ATUMS training program is supported by NSERC CREATE and is thanked for continued generous financial support (CREATE-463990-2015). Part of the research described in this paper was performed at the Canadian Light Source, a national research facility of the University of Saskatchewan, which is supported by the Canada Foundation for Innovation (CFI), the Natural Sciences and Engineering Research Council (NSERC), the National Research Council (NRC), the Canadian Institutes of Health Research (CIHR), the Government of Saskatchewan, and the University of Saskatchewan.

## REFERENCES

- (1) Samsung Newsroom. [NEXT for QLED] Part 1: Samsung Dominates the Large Screen TV Market. <https://news.samsung.com/global/next-for-qled-part-1-samsung-dominates-the-large-screen-tv-market> (accessed 2020-06-26).
- (2) Halford, B. Quantum dot LEDs go cadmium-free. *Chem. Eng. News* **2019**, 97. <https://cen.acs.org/materials/electronic-materials/Quantum-dot-LEDs-cadmium-free/97/i47>.
- (3) Union, T. E., Ed. *Publications Office of the European Union: Official Journal of the European Union*, 2017; Vol. 2017/1975, p 3.
- (4) Program, N. T. *NTP Technical Report on the Toxicology and Carcinogenesis Studies of Indium Phosphide in F344/N Rats and B6C3F1 Mice (Inhalation Studies)*; U.S. Department of Health and Human Services, July 2001.
- (5) Nanoco. <https://www.nanocotechnologies.com/> (accessed 2020-06-26).
- (6) Veinot, J. G. C. Synthesis, surface functionalization, and properties of freestanding silicon nanocrystals. *Chem. Commun.* **2006**, 40, 4160–4168.
- (7) Mangolini, L.; Kortshagen, U. Plasma-assisted synthesis of silicon nanocrystal inks. *Adv. Mater.* **2007**, 19 (18), 2513–2519.
- (8) Tilley, R. D.; Warner, J. H.; Yamamoto, K.; Matsui, I.; Fujimori, H. Micro-emulsion synthesis of monodisperse surface stabilized silicon nanocrystals. *Chem. Commun.* **2005**, 14, 1833–1835.
- (9) Baldwin, R. K.; Pettigrew, K. A.; Ratai, E.; Augustine, M. P.; Kauzlarich, S. M. Solution reduction synthesis of surface stabilized silicon nanoparticles. *Chem. Commun.* **2002**, 17, 1822–1823.
- (10) Zou, J.; Kauzlarich, S. M. Functionalization of Silicon Nanoparticles via Silanization: Alkyl, Halide and Ester. *J. Cluster Sci.* **2008**, 19 (2), 341–355.
- (11) Yang, Z.; Gonzalez, C. M.; Purkait, T. K.; Iqbal, M.; Meldrum, A.; Veinot, J. G. Radical Initiated Hydrosilylation on Silicon Nanocrystal Surfaces: An Evaluation of Functional Group Tolerance and Mechanistic Study. *Langmuir* **2015**, 31 (38), 10540–10548.
- (12) Liu, X.; Zhao, S.; Gu, W.; Zhang, Y.; Qiao, X.; Ni, Z.; Pi, X.; Yang, D. Light-Emitting Diodes Based on Colloidal Silicon Quantum Dots with Octyl and Phenylpropyl Ligands. *ACS Appl. Mater. Interfaces* **2018**, 10 (6), 5959–5966.
- (13) Meinardi, F.; Ehrenberg, S.; Dharmo, L.; Carulli, F.; Mauri, M.; Bruni, F.; Simonutti, R.; Kortshagen, U.; Brovelli, S. Highly efficient luminescent solar concentrators based on earth-abundant indirect-bandgap silicon quantum dots. *Nat. Photonics* **2017**, 11, 177–185.
- (14) Mazzaro, R.; Gradone, A.; Angeloni, S.; Morselli, G.; Cozzi, P. G.; Romano, F.; Vomiero, A.; Ceroni, P. Hybrid Silicon Nanocrystals for Color-Neutral and Transparent Luminescent Solar Concentrators. *ACS Photonics* **2019**, 6 (9), 2303–2311.
- (15) Erogbogbo, F.; Yong, K.-T.; Roy, I.; Hu, R.; Law, W.-C.; Zhao, W.; Ding, H.; Wu, F.; Kumar, R.; Swihart, M. T.; Prasad, P. N. In Vivo Targeted Cancer Imaging, Sentinel Lymph Node Mapping and Multi-Channel Imaging with Biocompatible Silicon Nanocrystals. *ACS Nano* **2011**, 5 (1), 413–423.
- (16) Tu, C.; Ma, X.; House, A.; Kauzlarich, S. M.; Louie, A. Y. PET Imaging and Biodistribution of Silicon Quantum Dots in Mice. *ACS Med. Chem. Lett.* **2011**, 2 (4), 285–288.
- (17) Gonzalez, C. M.; Iqbal, M.; Dasog, M.; Piercey, D. G.; Lockwood, R.; Klapotke, T. M.; Veinot, J. G. C. Detection of high-energy compounds using photoluminescent silicon nanocrystal paper based sensors. *Nanoscale* **2014**, 6 (5), 2608–2612.
- (18) Gonzalez, C. M.; Veinot, J. G. C. Silicon nanocrystals for the development of sensing platforms. *J. Mater. Chem. C* **2016**, 4 (22), 4836–4846.
- (19) Kim, H.; Seo, M.; Park, M. H.; Cho, J. A critical size of silicon nano-anodes for lithium rechargeable batteries. *Angew. Chem., Int. Ed.* **2010**, 49 (12), 2146–2149.
- (20) Su, X.; Wu, Q.; Li, J.; Xiao, X.; Lott, A.; Lu, W.; Sheldon, B. W.; Wu, J. Silicon-Based Nanomaterials for Lithium-Ion Batteries: A Review. *Adv. Energy Mater.* **2014**, 4 (1), 1300882.
- (21) Dasog, M.; De los Reyes, G. B.; Titova, L. V.; Hegmann, F. A.; Veinot, J. G. C. Size vs surface: tuning the photoluminescence of freestanding silicon nanocrystals across the visible spectrum via surface groups. *ACS Nano* **2014**, 8 (9), 9636–48.
- (22) Mobarok, M. H.; Purkait, T. K.; Islam, M. A.; Miskolzie, M.; Veinot, J. G. C. Instantaneous Functionalization of Chemically Etched Silicon Nanocrystal Surfaces. *Angew. Chem., Int. Ed.* **2017**, 56 (22), 6073–6077.
- (23) Islam, M. A.; Mobarok, M. H.; Sinelnikov, R.; Purkait, T. K.; Veinot, J. G. C. Phosphorus Pentachloride Initiated Functionalization of Silicon Nanocrystals. *Langmuir* **2017**, 33 (35), 8766–8773.
- (24) Sangghaleh, F.; Sychugov, I.; Yang, Z.; Veinot, J. G. C.; Linnros, J. Near-Unity Internal Quantum Efficiency of Luminescent Silicon Nanocrystals with Ligand Passivation. *ACS Nano* **2015**, 9 (7), 7097–7104.
- (25) Jurbergs, D.; Rogojina, E.; Mangolini, L.; Kortshagen, U. Silicon nanocrystals with ensemble quantum yields exceeding 60%. *Appl. Phys. Lett.* **2006**, 88 (23), 233116.
- (26) Wheeler, L. M.; Anderson, N. C.; Palomaki, P. K. B.; Blackburn, J. L.; Johnson, J. C.; Neale, N. R. Silyl Radical Abstraction in the

Functionalization of Plasma-Synthesized Silicon Nanocrystals. *Chem. Mater.* **2015**, *27* (19), 6869–6878.

(27) Ddungu, J. L. Z.; Silvestrini, S.; Tassoni, A.; De Cola, L. Shedding Light on the Aqueous Synthesis of Silicon Nanoparticles by Reduction of Silanes with Citrates. *Faraday Discuss.* **2020**, *222*, 350.

(28) Dasog, M.; Yang, Z. Y.; Regli, S.; Atkins, T. M.; Faramus, A.; Singh, M. P.; Muthuswamy, E.; Kauzlarich, S. M.; Tilley, R. D.; Veinot, J. G. C. Chemical Insight into the Origin of Red and Blue Photoluminescence Arising from Freestanding Silicon Nanocrystals. *ACS Nano* **2013**, *7* (3), 2676–2685.

(29) Sinelnikov, R.; Dasog, M.; Beamish, J.; Meldrum, A.; Veinot, J. G. C. Revisiting an Ongoing Debate: What Role Do Surface Groups Play in Silicon Nanocrystal Photoluminescence? *ACS Photonics* **2017**, *4* (8), 1920–1929.

(30) Rodríguez, J. A.; Vásquez-Agustín, M. A.; Morales-Sánchez, A.; Aceves-Mijares, M. Emission Mechanisms of Si Nanocrystals and Defects in SiO<sub>2</sub> Materials. *J. Nanomater.* **2014**, *2014*, 409482.

(31) Canham, L. T. Luminescence Bands and their Proposed Origins In Highly Porous Silicon. *Phys. Status Solidi B* **1995**, *190*, 9–14.

(32) Lee, B. G.; Luo, J.-W.; Neale, N. R.; Beard, M. C.; Hiller, D.; Zacharias, M.; Stradins, P.; Zunger, A. Quasi-Direct Optical Transitions in Silicon Nanocrystals with Intensity Exceeding the Bulk. *Nano Lett.* **2016**, *16* (3), 1583–1589.

(33) Mazzaro, R.; Romano, F.; Ceroni, P. Long-lived Luminescence of Silicon Nanocrystals: From Principles to Applications. *Phys. Chem. Chem. Phys.* **2017**, *19* (39), 26507–26526.

(34) DeBenedetti, W. J. I.; Chiu, S.-K.; Radlinger, C. M.; Ellison, R. J.; Manhat, B. A.; Zhang, J. Z.; Shi, J.; Goforth, A. M. Conversion from Red to Blue Photoluminescence in Alcohol Dispersions of Alkyl-Capped Silicon Nanoparticles: Insight into the Origins of Visible Photoluminescence in Colloidal Nanocrystalline Silicon. *J. Phys. Chem. C* **2015**, *119* (17), 9595–9608.

(35) Dasog, M.; Bader, K.; Veinot, J. G. C. Influence of Halides on the Optical Properties of Silicon Quantum Dots. *Chem. Mater.* **2015**, *27* (4), 1153–1156.

(36) Li, X.; He, Y.; Talukdar, S. S.; Swihart, M. T. Process for Preparing Macroscopic Quantities of Brightly Photoluminescent Silicon Nanoparticles with Emission Spanning the Visible Spectrum. *Langmuir* **2003**, *19* (20), 8490–8496.

(37) Hessel, C. M.; Reid, D.; Panthani, M. G.; Rasch, M. R.; Goodfellow, B. W.; Wei, J.; Fujii, H.; Akhavan, V.; Korgel, B. A. Synthesis of Ligand-Stabilized Silicon Nanocrystals with Size-Dependent Photoluminescence Spanning Visible to Near-Infrared Wavelengths. *Chem. Mater.* **2012**, *24* (2), 393–401.

(38) Niquet, Y. M.; Delerue, C.; Allan, G.; Lannoo, M. Method for Tight-binding Parametrization: Application to Silicon Nanostructures. *Phys. Rev. B: Condens. Matter Mater. Phys.* **2000**, *62* (8), 5109–5116.

(39) Yu, Y.; Fan, G.; Fermi, A.; Mazzaro, R.; Morandi, V.; Ceroni, P.; Smilgies, D.-M.; Korgel, B. A. Size-Dependent Photoluminescence Efficiency of Silicon Nanocrystal Quantum Dots. *J. Phys. Chem. C* **2017**, *121* (41), 23240–23248.

(40) Jia, X.; Zhang, P.; Lin, Z.; Anthony, R.; Kortshagen, U.; Huang, S.; Puthen-Veetil, B.; Conibeer, G.; Perez-Wurfl, I. Accurate Determination of the Size Distribution of Si Nanocrystals from PL Spectra. *RSC Adv.* **2015**, *5* (68), 55119–55125.

(41) de Boer, W. D. A. M.; Timmerman, D.; Dohnalová, K.; Yassievich, I. N.; Zhang, H.; Buma, W. J.; Gregorkiewicz, T. Red Spectral Shift and Enhanced Quantum Efficiency in Phonon-Free Photoluminescence from Silicon Nanocrystals. *Nat. Nanotechnol.* **2010**, *5* (12), 878–884.

(42) Delerue, C.; Allan, G.; Lannoo, M. Theoretical Aspects of the Luminescence of Porous Silicon. *Phys. Rev. B: Condens. Matter Mater. Phys.* **1993**, *48* (15), 11024–11036.

(43) Wang, L. W.; Zunger, A. Electronic Structure Pseudopotential Calculations of Large (approx.1000 Atoms) Si Quantum Dots. *J. Phys. Chem.* **1994**, *98* (8), 2158–2165.

(44) Hill, N. A.; Whaley, K. B. Size Dependence of Excitons in Silicon Nanocrystals. *Phys. Rev. Lett.* **1995**, *75* (6), 1130–1133.

(45) Hill, N. A.; Whaley, K. B. A Theoretical Study of Light Emission from Nanoscale Silicon. *J. Electron. Mater.* **1996**, *25* (2), 269–285.

(46) Ögüt, S.; Chelikowsky, J. R.; Louie, S. G. Quantum Confinement and Optical Gaps in Si Nanocrystals. *Phys. Rev. Lett.* **1997**, *79* (9), 1770–1773.

(47) Liu, S.-M.; Yang, S.; Sato, S.; Kimura, K. Enhanced Photoluminescence from Si Nano-organosols by Functionalization with Alkenes and Their Size Evolution. *Chem. Mater.* **2006**, *18* (3), 637–642.

(48) Mastronardi, M. L.; Maier-Flaig, F.; Faulkner, D.; Henderson, E. J.; Kübel, C.; Lemmer, U.; Ozin, G. A. Size-Dependent Absolute Quantum Yields for Size-Separated Colloidally-Stable Silicon Nanocrystals. *Nano Lett.* **2012**, *12* (1), 337–342.

(49) Hannah, D. C.; Yang, J.; Podsiadlo, P.; Chan, M. K. Y.; Demortière, A.; Gosztola, D. J.; Prakupenka, V. B.; Schatz, G. C.; Kortshagen, U.; Schaller, R. D. On the Origin of Photoluminescence in Silicon Nanocrystals: Pressure-Dependent Structural and Optical Studies. *Nano Lett.* **2012**, *12* (8), 4200–4205.

(50) Wen, X.; Zhang, P.; Smith, T. A.; Anthony, R. J.; Kortshagen, U. R.; Yu, P.; Feng, Y.; Shrestha, S.; Coniber, G.; Huang, S. Tunability Limit of Photoluminescence in Colloidal Silicon Nanocrystals. *Sci. Rep.* **2015**, *5* (1), 12469.

(51) Jakob, M.; Javadi, M.; Veinot, J. G. C.; Meldrum, A.; Kartouzian, A.; Heiz, U. Ensemble Effects in the Temperature-Dependent Photoluminescence of Silicon Nanocrystals. *Chem. - Eur. J.* **2019**, *25* (12), 3061–3067.

(52) Breiteneker, M.; Sixel, R.; Thirring, W. On the effective mass approximation. *Eur. Phys. J. A* **1964**, *182* (2), 123–129.

(53) Hannah, D. C.; Yang, J.; Kramer, N. J.; Schatz, G. C.; Kortshagen, U. R.; Schaller, R. D. Ultrafast Photoluminescence in Quantum-Confined Silicon Nanocrystals Arises from an Amorphous Surface Layer. *ACS Photonics* **2014**, *1* (10), 960–967.

(54) Kúsová, K.; Ondič, L.; Pelant, I. Comment on “Ultrafast Photoluminescence in Quantum-Confined Silicon Nanocrystals Arises from an Amorphous Surface Layer”. *ACS Photonics* **2015**, *2* (3), 454–455.

(55) Hannah, D. C.; Yang, J.; Kramer, N. J.; Schatz, G. C.; Kortshagen, U. R.; Schaller, R. D. Reply to “Comment on ‘Ultrafast Photoluminescence in Quantum-Confined Silicon Nanocrystals Arises from an Amorphous Surface Layer’”. *ACS Photonics* **2015**, *2* (3), 456–458.

(56) Brown, S. L.; Miller, J. B.; Anthony, R. J.; Kortshagen, U. R.; Kryjevski, A.; Hobbie, E. K. Abrupt Size Partitioning of Multimodal Photoluminescence Relaxation in Monodisperse Silicon Nanocrystals. *ACS Nano* **2017**, *11* (2), 1597–1603.

(57) Thiessen, A. N.; Ha, M.; Hooper, R. W.; Yu, H.; Olynyk, A. O.; Veinot, J. G. C.; Michaelis, V. K. Silicon Nanoparticles: Are They Crystalline from the Core to the Surface? *Chem. Mater.* **2019**, *31* (3), 678–688.

(58) Jarolimek, K.; Hazrati, E.; de Groot, R. A.; de Wijs, G. A. Band Offsets at the Interface between Crystalline and Amorphous Silicon from First Principles. *Phys. Rev. Appl.* **2017**, *8* (1), 014026.

(59) Hessel, C. M.; Henderson, E. J.; Veinot, J. G. C. Hydrogen Silsesquioxane: A Molecular Precursor for Nanocrystalline Si-SiO<sub>2</sub> Composites and Freestanding Hydride-Surface-Terminated Silicon Nanoparticles. *Chem. Mater.* **2006**, *18* (26), 6139–6146.

(60) Hessel, C. M.; Henderson, E. J.; Veinot, J. G. C. An Investigation of the Formation and Growth of Oxide-Embedded Silicon Nanocrystals in Hydrogen Silsesquioxane-Derived Nanocomposites. *J. Phys. Chem. C* **2007**, *111* (19), 6956–6961.

(61) Clark, R. J.; Aghajamali, M.; Gonzalez, C. M.; Hadidi, L.; Islam, M. A.; Javadi, M.; Mobarok, M. H.; Purkait, T. K.; Robidillo, C. J. T.; Sinelnikov, R.; Thiessen, A. N.; Washington, J.; Yu, H.; Veinot, J. G. C. From Hydrogen Silsesquioxane to Functionalized Silicon Nanocrystals. *Chem. Mater.* **2017**, *29* (1), 80–89.

(62) Dohnalova, K.; Gregorkiewicz, T.; Kusova, K. Silicon quantum dots: surface matters. *J. Phys.: Condens. Matter* **2014**, *26* (17), 173201.

(63) Balzar, D.; Audebrand, N.; Daymond, M. R.; Fitch, A.; Hewat, A.; Langford, J. I.; Le Bail, A.; Louër, D.; Masson, O.; McCowan, C. N.; Popa, N. C.; Stephens, P. W.; Toby, B. H. Size-strain line-broadening analysis of the ceria round-robin sample. *J. Appl. Crystallogr.* **2004**, *37* (6), 911–924.

(64) Jakob, M.; Aissiou, A.; Morrish, W.; Marsiglio, F.; Islam, M.; Kartouzian, A.; Meldrum, A. Reappraising the Luminescence Lifetime Distributions in Silicon Nanocrystals. *Nanoscale Res. Lett.* **2018**, *13* (1), 383.

(65) Dabbousi, B. O.; Rodriguez-Viejo, J.; Mikulec, F. V.; Heine, J. R.; Mattoussi, H.; Ober, R.; Jensen, K. F.; Bawendi, M. G. (CdSe)ZnS Core-Shell Quantum Dots: Synthesis and Characterization of a Size Series of Highly Luminescent Nanocrystallites. *J. Phys. Chem. B* **1997**, *101* (46), 9463–9475.

(66) Lee, B. G.; Hiller, D.; Luo, J. W.; Semonin, O. E.; Beard, M. C.; Zacharias, M.; Stradins, P. Strained Interface Defects in Silicon Nanocrystals. *Adv. Funct. Mater.* **2012**, *22* (15), 3223–3232.

(67) Kleovoulou, K.; Kelires, P. C. Stress state of embedded Si nanocrystals. *Phys. Rev. B: Condens. Matter Mater. Phys.* **2013**, *88*, 085424.

(68) Delerue, C.; Allan, G.; Reynaud, C.; Guillois, O.; Ledoux, G.; Huisken, F. Multiexponential Photoluminescence Decay in Indirect-Gap Semiconductor Nanocrystals. *Phys. Rev. B: Condens. Matter Mater. Phys.* **2006**, *73* (23), 235318.

(69) Miller, J. B.; Van Sickle, A. R.; Anthony, R. J.; Kroll, D. M.; Kortshagen, U. R.; Hobbie, E. K. Ensemble Brightening and Enhanced Quantum Yield in Size-Purified Silicon Nanocrystals. *ACS Nano* **2012**, *6* (8), 7389–7396.

(70) Huisken, F.; Ledoux, G.; Guillois, O.; Reynaud, C. Light-Emitting Silicon Nanocrystals from Laser Pyrolysis. *Adv. Mater.* **2002**, *14* (24), 1861–1865.

(71) Belyakov, V. A.; Burdov, V. A.; Gaponova, D. M.; Mikhaylov, A. N.; Tetelbaum, D. I.; Trushin, S. A. Phonon-Assisted Radiative Electron-Hole Recombination in Silicon Quantum Dots. *Phys. Solid State* **2004**, *46*, 27–31.

(72) Belyakov, V. A.; Burdov, V. A.; Lockwood, R.; Meldrum, A. Silicon Nanocrystals: Fundamental Theory and Implications for Stimulated Emission. *Adv. Opt. Technol.* **2008**, *2008*, 279502.

(73) Lannoo, M.; Delerue, C.; Allan, G. Nonradiative Recombination on Dangling Bonds in Silicon Crystallites. *J. Lumin.* **1993**, *57* (1), 243–247.

(74) Bae, W. K.; Padilha, L. A.; Park, Y.-S.; McDaniel, H.; Robel, I.; Pietryga, J. M.; Klimov, V. I. Controlled Alloying of the Core-Shell Interface in CdSe/CdS Quantum Dots for Suppression of Auger Recombination. *ACS Nano* **2013**, *7* (4), 3411–3419.

(75) Anderson, S. L.; Lubber, E. J.; Olsen, B. C.; Buriak, J. M. Substance over Subjectivity: Moving beyond the Histogram. *Chem. Mater.* **2016**, *28* (17), 5973–5975.

(76) Kilaas, R. Optimal and near-optimal filters in high-resolution electron microscopy. *J. Microsc.* **1998**, *190*, 45–51.